Aerodynamic behavior of a gas mask canister containing two porous media

Chun-Chi Li*

Department of Mechatronic, Energy and Aerospace Engineering, Chung Cheng Institute of Technology, National Defense University, No. 190, Sanyuan 1st St., Dasi Township 335, Taoyuan County, Taiwan, ROC

ABSTRACT

This paper discusses the aerodynamic behaviors of a gas mask canister with a complex inner structure and two porous materials in the filter layer and the activated carbon layer. The effects of the distribution and area of holes in the main sieve diaphragm and the thickness of the activated carbon layer on the pressure drop and the flow structure were determined using computational fluid dynamic (CFD) tools. The momentum loss of porous flow calculated by Forchheimer's equation was added to the source term in the momentum equation. Streakline flow visualization was employed to observe gas flow structures within the empty canister and to identify the shortcomings of the prototype canister. Simulation results for the estimated inertial and viscosity parameters in Forchheimer's equation agree closely with experimental values. The porosity of the canister for intake flows of 15–135 L/min causes the flow behavior to transition gradually from linear (viscous effect) to slight non-linear behavior (slight inertia effect). This study uses air age as an index of the time that air resides within the canister to displace the adsorption time of toxic gas. This approach conveniently elucidates overall filter capacity and the positions of dead zones in the activated carbon layer. The simulation results reveal that the channel design of the main sieve diaphragm dominates the aerodynamic behavior of the fluid within the activated carbon layer. Better hole distribution and a larger hole area correspond to a lower pressure drop, a smaller dead zone, and a higher adsorption time. The results in this study provide a valuable reference for designing channels in the main sieve diaphragm, and will be helpful in designing gas mask canisters.

© 2009 Elsevier Ltd. All rights reserved.

1. Introduction

After the September 11 terrorist attacks on the World Trade Center in New York, a series of anthrax powder threats caused global anxiety. This type of threat caused an unexpected surge in gas mask sales. Improving the performance of gas masks therefore not only enhances personal safety, but also represents a huge commercial opportunity. The toxin-filtering function of a gas mask depends on the canister attached, which filters aerosols and absorbs toxic gases. Gas mask canisters typically consist of a filter layer and an activated porous carbon layer that can efficiently block particles (e.g. anthrax), chemical agents (e.g. nerve gas), and germs (e.g. smallpox). The American National Institute of Occupational Safety and Health (NIOSH) and the US Army standard for general canisters both require that solid particles larger than 0.3 μm be filtered. Canisters are categorized according to the efficiency with which they remove aerosol spray (toxic gas or droplet): 95%, 99% or 99.97% (Fischetti, 2002). Requirements for the next-generation M50 JSGPM mask developed by the US Army state that weight and respiratory resistance must be 50% lower than for the M40 series masks currently in service.

This study analyzes a canister that has been marketed since 1970 that has a filter capacity that meets the NIOSH 99.97% standard. However, its shortcomings are too heavy (330 g) and a high respiratory drag factor. At an inspiration flow rate of 30 L/min, the measured pressure drop is about 200 Pa. The canister is 20% heavier than a similar product (Scott NBC22), and its pressure drop is 40% higher.

The canister's internal configuration (Fig. 1(a)) is very complex. The bracket helps support the filter layer, which comprises multi-pleated filter papers that trap large suspended aerosol particles. The main sieve diaphragm separates the filter layer from the activated carbon layer, and its structural strength alleviates the strain on the activated carbon layer during high stress movements. This design prevents gaps that can result in the loss of activated carbon particles due to deformation, which in turn can cause canister failure. The main sieve diaphragm has several holes of various diameters, ranging from 4 to 7 mm. These holes allow gas to pass through the filter layer into the activated carbon layer. In the original design, the outermost-ring holes in the main sieve diaphragm are sealed to prevent glue from migrating into the activated carbon layer during packing, as Fig. 1(b) shows. The type of glue used is

* Tel.: +886 3 3803043; fax: +886 3 3893475.
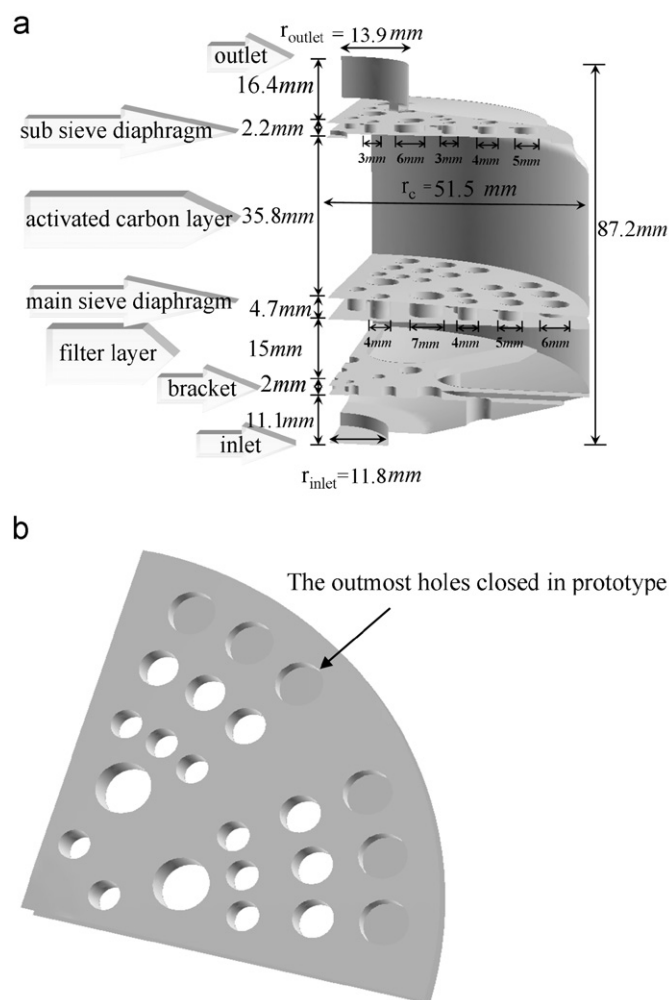*E-mail addresses:* davidli@ndu.edu.tw, davidli@ccit.edu.tw.

Fig. 1. (a) Dimensions of gas mask canister and components and (b) configuration of main sieve diaphragm.

Table 1
Main physical characteristics of the filter layer and activated carbon layer.

Filter layer	
Pleated number	36
Material	Polypropylene melt-blown non-woven
Activated carbon layer	
Carbonization temperature (°C)	1000
Activation process	H_2O
Particle diameter (mm)	0.70–0.90
Density ($g\,m^{-3}$)	0.40–0.50
Porous volume ($cm^3\,g^{-1}$)	> 0.5
BET surface area ($m^2\,g^{-1}$)	> 1000
Water content (%)	< 5
Ash content (%)	< 10
Microporous volume ($cm^3\,g^{-1}$)	> 0.32

polyurethane (PU); its function is to seal around the canister so that the activated carbon particles will not permeate into the filter layer. The activated carbon layer comprises activated carbon particles that absorb and filter toxic gases. The sub-sieve diaphragm prevents activated carbon particles from entering the canister outlet. The main physical characteristics of the filter paper and activated carbon particles are given in Table 1.

In common gas mask canisters, the mean inhalation flow rate varies from 15 L/min at rest to 135 L/min for intense exercise (Wang

and Wang, 2003). Standard tests measure the pressure drop at a flow rate of 30 L/min. For the canister investigated in the present study, the entry Reynolds numbers (approx. 900–8100) calculated from the inhalation flow rates indicate that turbulent effects in the inflow should be analyzed.

This study uses fluid dynamics to analyze the aerodynamic behavior of the filter and activated carbon layers in the canister. These layers are porous media that cause a considerable pressure drop. In 1856, Darcy first derived an equation to describe the momentum dissipation of a fluid flowing through a porous medium (Dullien, 1979):

$$-\frac{\Delta p}{L} = \frac{\mu}{\kappa} V_s, \tag{1}$$

where ΔP is the pressure drop of the porous medium zone; L is the length of the flow direction; κ is the permeability; μ is the fluid viscosity, and V_s denotes the superficial velocity of the fluid entering the porous medium zone. Darcy's equation considers only the viscosity effect. A corrective convection term must be added to consider the inertia effect. This addition yields Forchheimer's equation (Dullien, 1979)

$$-\frac{\Delta p}{L} = \alpha \mu V_s + \beta \rho V_s^2, \tag{2}$$

where α is the reciprocal permeability of the porous material, or viscosity parameter. β is usually called the inertial parameter. Forchheimer's equation describes the relationship between the global pressure drop in the porous media zone and the superficial velocity on a macroscopic perspective. A higher superficial velocity corresponds to a greater pressure drop. The factors α, β, L and V_s determine the pressure drop. When the superficial velocity V_s is very low or the Reynolds number is small, the inertia effect is far smaller than the viscosity effect. As the Reynolds number increases, the flow characteristics of the porous media gradually change from linear (Darcy's equation) to non-linear (Forchheimer's equation). This behavior differs from the general flow behavior, which involves an instantaneous change from laminar to turbulent flow (Dullien, 1979). The non-dimensional form of Eq. (2) is

$$f = \frac{1}{Re'} + 1, \tag{3}$$

where $f \equiv -\Delta p / L \beta \rho V_s^2$, and $Re' \equiv \beta \rho V_s / \alpha \mu$. This equation is called the friction factor–Reynolds number form equation (Andrada et al., 1999). This equation can be used to analyze linear to non-linear changes in porous media flow characteristics under various flow conditions.

Aerodynamic behaviors, including pressure drops and flow structure, are important considerations in the design of porous filters (Subrenat et al., 2000, 2003). Flow structures affect gas treatment processes within the filter by preventing preferential flow (which leads to absorbent failure due to overuse) and the formation of a dead zone (which leads to absorbent waste due to fluid not passage). Since the absorbent is opaque, the inner flow structures cannot be visually examined in terms of the size and location of preferential flow and dead zones. However, exploring the aerodynamic characteristics of a flow field using computational fluid dynamic (CFD) tools is helpful in analyzing the flow variables in porous media within a filter (Chen et al., 1995; Liu and Wang, 1996). The gas residence time in the filter must also be considered to ensure that the filter's absorption capacity is fully exploited. This study uses an air age index to determine whether or not overall filtering capacity is maintained after the canister body's structure has been changed. A greater air age value corresponds to a longer air residence time. A lower air age value represents fresher air (Li et al., 2003). Air residence time distribution can therefore be used to optimize the geometry of industrial filters (Baléo and Le Cloirec, 2000a, 2000b). This approach

conveniently elucidates overall filter capacity and the positions of dead zones in the activated carbon layer.

Previous authors have used CFD tools to analyze porous filters, but their primary focus was to analyze the fluids flow through different arrays of the spatial microstructure of a filter media in 2- or 3-D simulations (Dhaniyala and Liu, 1999; Liu and Wang, 1996; Thomas et al., 1999). The geometrical design of particular filters, such as cylindrical pleated filters, was another purpose for using the pleating effect to design a new industrial filter (Baléo et al. 2000; Subrenat et al. 2000, 2001, 2003). The point which most previous studies have in common is that they focused on a single type of porous media. However, very little existing literature analyzes the aerodynamic characteristics of a gas mask canister. Therefore, the topic of the aerodynamic behavior of a gas mask canister with two kinds porous materials is worthy of further research.

The purpose of this study is to evaluate the aerodynamic behaviors of a gas mask canister in an attempt to decrease its pressure drag and overall weight. A streamline flow visualization reveals the flow phenomena of gas entering the empty canister as the outermost holes on the main sieve diaphragm open and close. Observations of this behavior were then compared to computational results to identify any problems with the prototype canister design. The pressure drops for the filter and activated carbon layers were then experimentally measured at different inlet Reynolds numbers. The Forchheimer coefficients in Eq. (2) are determined from measured values of pressure drop and velocity in either the filter layer or the activated carbon layer under different flow rates. The results for the porous media and compared to computational results to verify their accuracy and the effectiveness of the computational program. The aerodynamic behaviors of the canister were investigated for a range of inhalation flow rates by simulating different hole distributions and areas on the main sieve diaphragm, the thickness of the activated carbon layer, and the air age index.

2. Problem

2.1. Governing equations

The governing equations herein include the continuity and momentum equations, both of which obey the conservation principle (Subrenat et al., 2003),

$$\frac{\partial}{\partial x_i}(\rho u_i) = 0, \tag{4}$$

$$\frac{\partial}{\partial x_j}(\rho u_i u_j) = -\frac{\partial p}{\partial x_i} + \frac{\partial \tau_{ij}}{\partial x_j} + \rho g_i - \frac{\partial}{\partial x_j}(\rho \overline{u_i' u_j'}) + S_i, \tag{5}$$

where ρ is the gas density; u_i is the velocity component in direction i. The momentum Eq. (5) are steady, 3-D Reynolds-averaged Navier–Stoke's equations, p is the pressure; τ_{ij} is the viscosity shear stress tensor; g_i is the acceleration due to gravity in direction i. The direction of the gravity term is perpendicular with the canister inlet, which is the axial direction (the opposite direction of z). When the flow is not laminar, the Reynolds stress term $\rho \overline{u_i' u_j'}$ is related to the mean flow by the Boussinesq hypothesis. The source term S_i describes the pressure gradient in the porous medium, and is given by Eq. (2) and is assumed to be isotropic. The inlet Reynolds number ranges from 900 to 8100, so this study adopts a modified low-Reynolds number k–ε turbulent model (Jones and Launder, 1973). The working gas is air, for which $\rho = 1.225 \, \text{kg m}^{-3}$ and $\mu = 1.7894 \times 10^{-5} \, \text{kg m}^{-1} \, \text{s}^{-1}$.

The air age equation (Li et al., 2003) is

$$\frac{\partial}{\partial x_i}(\rho u_i \tau) = \frac{\partial}{\partial x_i}\left(\frac{\mu_{eff}}{\sigma_\tau}\frac{\partial \tau}{\partial x_i}\right) + \rho, \tag{6}$$
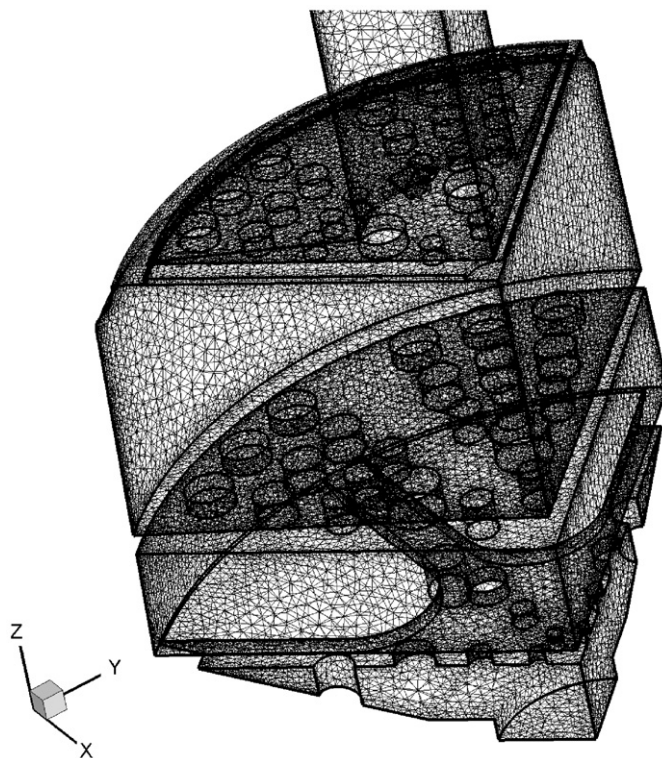

Fig. 2. Mesh system of prototype canister (model A_1).

where τ is the air age means the local average residence time; μ_{eff}/σ_τ is the local actual diffusivity in turbulent model; $\mu_{eff} = \mu_l + \mu_t$ (where μ_{eff} is effective viscosity, μ_l is molecular viscosity and μ_t is turbulent viscosity) and $\sigma_\tau = 1$ is the turbulent Schmidt number.

2.2. Boundary conditions

The canister inlet maintains a steady volumetric flow rate in all simulations. Since the inlet area is fixed, the calculated mean velocity is specified by the inlet boundary. A flow rate of 30 L/min, which is regarded as the mean inhalation flow rate of normal adults in light motion, serves as the reference value for subsequent simulations. The reference pressure is fixed at the inlet, with a value of 101,325 Pa. The outlet boundary condition is the pressure outlet boundary. The no-slip condition is assumed for all solid walls. For computational efficiency, only one-quarter of the full 3D model is constructed.

2.3. Numerical method

This study uses the FLUENT 6.2.16 flow solver, which is based on the finite volume method. The integral form of the governing equations is discretized using an unstructured tetrahedral grid. The convection term is discretized with the first-order upwind scheme and the viscosity term is discretized with a second-order central differential scheme. The SIMPLE algorithm (Patankar, 1980) is the solution algorithm for pressure–velocity coupling, and related discretization algebraic equations are solved using the TDMA method.

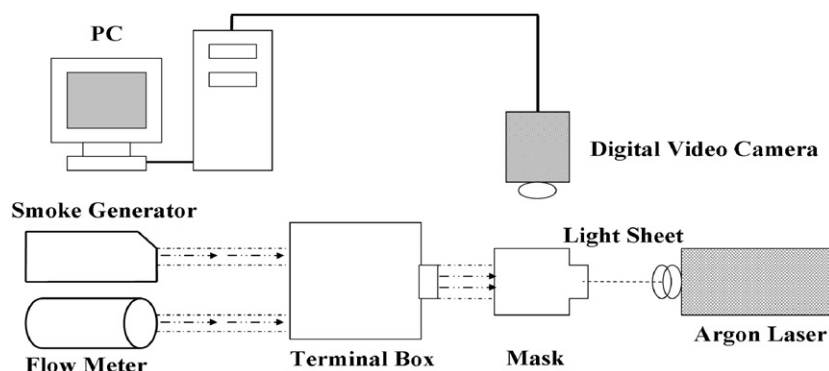### 2.4. Grid configuration and research matrix

Since the filter layer material is very light and causes a much lower pressure drop than the activated carbon layer, this study

Table 2
Research matrix.

Model	Parameter		
	Hole distribution: outmost holes of main sieve diaphragm opened: O and closed: X	Ratio of activated carbon layer thickness (note 1)	Hole area effect: magnification of holes size (note 2)
A			
A_1	X	1	1
A_2	O	1	1
B			
B_1	X	0.5	1
B_2	O	0.5	1
C			
C_1	X	0.25	1
C_2	O	0.25	1
D			
D_1	X	1	1.5
D_2	O	1	1.5
E			
E_1	X	0.5	1.5
E_2	O	0.5	1.5
F			
F_2	X	0.25	1.5
F_2	O	0.25	1.5
G			
G_1	X	1	0.8
G_2	O	1	0.8
H			
H_1	X	1	1.2
H_2	O	1	1.2

Note 1: the ratio of activated carbon layer thickness for model A is 1. The activated carbon layer thickness of model B and model C is 0.5 and 0.25 of model A, respectively.

Note 2: the hole size distributed on the main sieve diaphragm has a ratio of 1 in model A. The holes size for models D, G, H are 1.5, 0.8 and 1.2 times of model A, respectively.

Fig. 3. Schematic diagram of streakline flow visualization experiment.

focuses on the activated carbon layer. To simplify the computational domain, this study omits the effect of multi-pleated filter paper and treats the filter layer as a single layer. The medium of the two porous layers is assumed to be homogeneous. An unstructured tetrahedral mesh with a complex structure and self-adaptive characteristics is adopted. Local grids for the inlet, outlet, sieve diaphragm holes, and the activated carbon layer are refined to accurately capture the flow patterns. The domain is divided into 23 sub-domains, yielding a grid number of approximately 830,000 grids for the prototype. Fig. 2 displays the domain mesh. Grid distributions for the subsequent models were generated based on the prototype mesh. All the results presented in this study are grid insensitive. The residual convergence threshold in all cases is less than 1×10^{-4}.

The three most important parameters in determining the aerodynamic behavior of a gas mask canister are the distribution and area of holes on the main sieve diaphragm, and the thickness of the activated carbon layer. Table 2 presents the research matrix for more details.

3. Results and discussion

3.1. Flow observation and empty canister simulation

Before adopting CFD simulations, streakline visualizations were used to observe the flow structures of an empty canister without filter paper and activated carbon particles. The inlet flow rate was 30 L/min. The experimental set-up included an argon laser, a smoke generator, a flow meter, and a camcorder, as Fig. 3 shows. The results reveal that a large backflow zone forms when the outermost holes are sealed. As a result, the fluid does not flow to the outlet easily, as Fig. 4(a) illustrates. Computational results reveal a similar outcome (Fig. 4(b)). Both the experimental and the simulated results demonstrate that the backflow zone disappears when the outermost holes are open and the fluid can flow out smoothly, as Fig. 5(a) and (b) shows.

These results demonstrate that sealing the outermost holes in the main sieve diaphragm is a design flaw. When fluid flows actually through the activated carbon layer, the porous flow will not cause
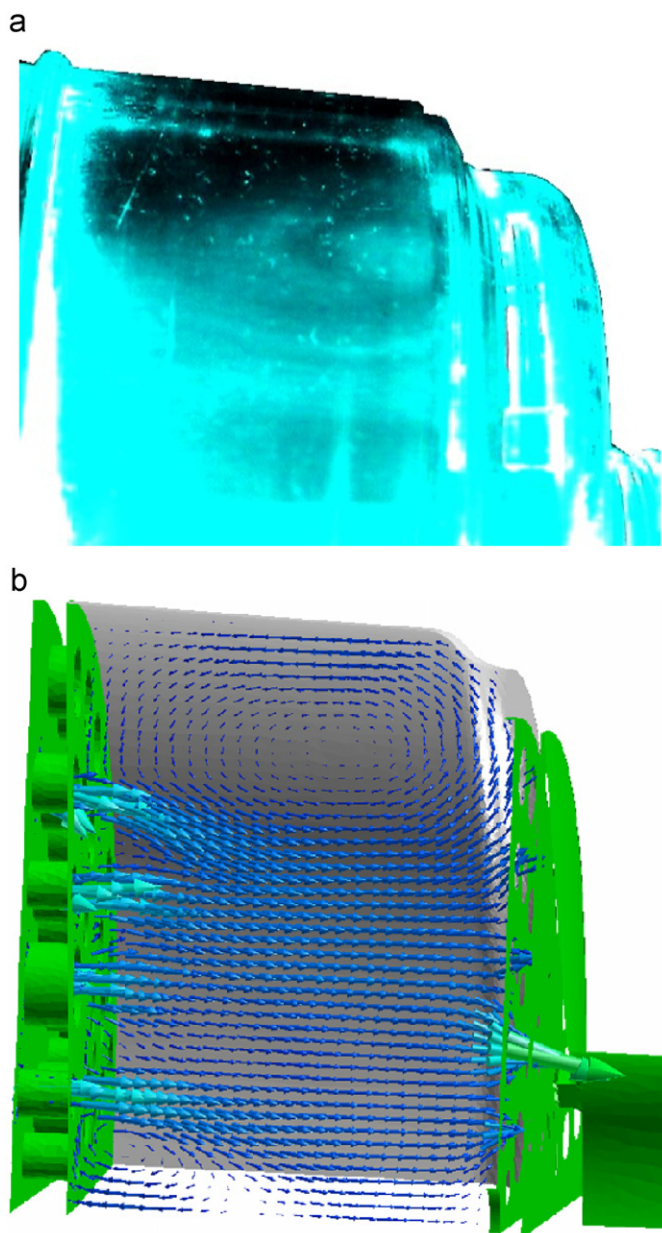
a

b

Fig. 4. (a) Experimental image of activated carbon region (without activated carbon particles) at a flow rate of 30 L/min (closed outermost holes on the main sieve diaphragm) and (b) simulated velocity vector of activated carbon region (without activated carbon particles) at a flow rate of 30 L/min (closed outermost holes on the main sieve diaphragm).

a

b

Fig. 5. (a) Experimental image of activated carbon region (without activated carbon particles) at a flow rate of 30 L/min (open outermost holes on the main sieve diaphragm) and (b) velocity vector for simulation of the activated carbon region (without activated carbon particles) at a flow rate of 30 L/min (open outermost holes on main sieve diaphragm).

backflow in the peripheral zone. However, if the fluid cannot flow into this zone easily, a dead zone forms. In turn, this reduces the flow-through area and increases both the superficial velocity and the pressure drop. Computational simulations verify this inference.

3.2. Porous medium parameters

The filter and the activated carbon layers in the porous media are responsible for the majority of the canister's pressure drop. As described above, Forchheimer's equation must be used to identify the characteristics of the porous medium, the viscosity, and inertial terms in the two regions.

This study built an experimental apparatus with a pressure difference transducer to measure the pressure at the inlet of the canister
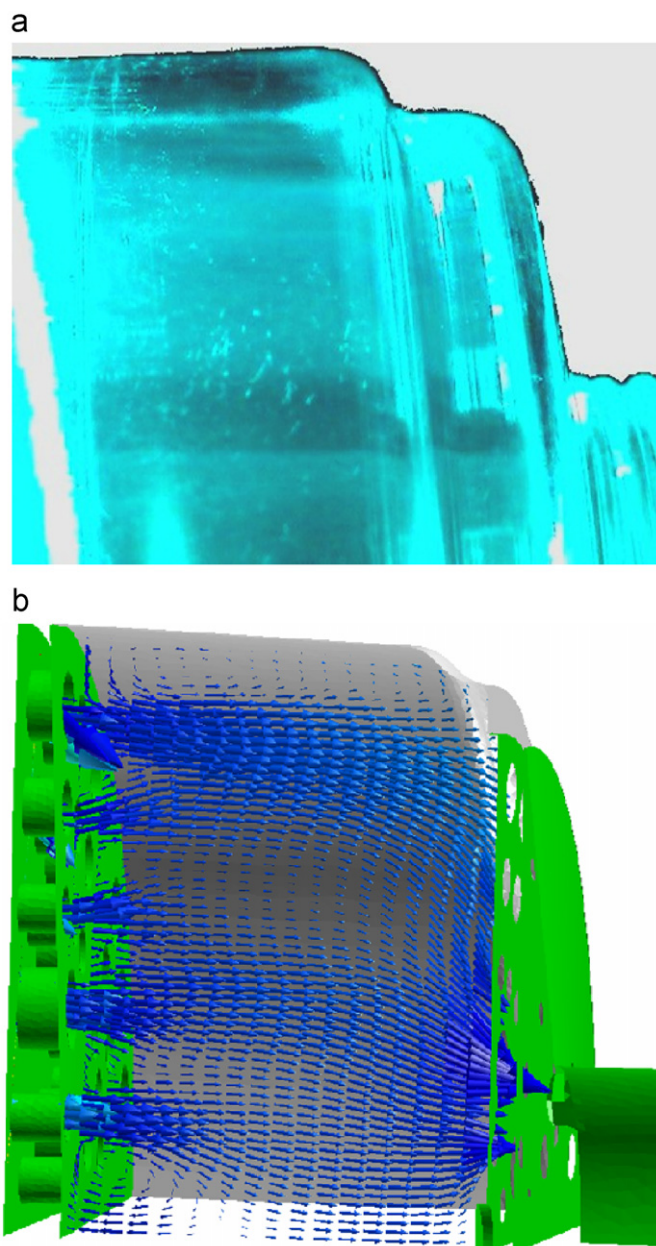
outlet ports. Curve fitting is used to obtain Forchheimer's equations for the filter layer and the activated carbon layer. The polynomial for the filter layer is

$$-\frac{\Delta P}{L_1} = \alpha_1 \mu V_s + \beta_1 \rho V_s^2 = 27143 V_s + 7849 V_s^2. \tag{7}$$

The polynomial for the activated carbon layer is

$$-\frac{\Delta P}{L_2} = \alpha_2 \mu V_s + \beta_2 \rho V_s^2 = 42744 V_s + 39284 V_s^2. \tag{8}$$

The following coefficients for the filter layer are determined as

$$\alpha_1 = 1.52 \times 10^9 \, \text{m}^{-2}, \quad \beta_1 = 6.41 \times 10^3 \, \text{m}^{-1}.$$

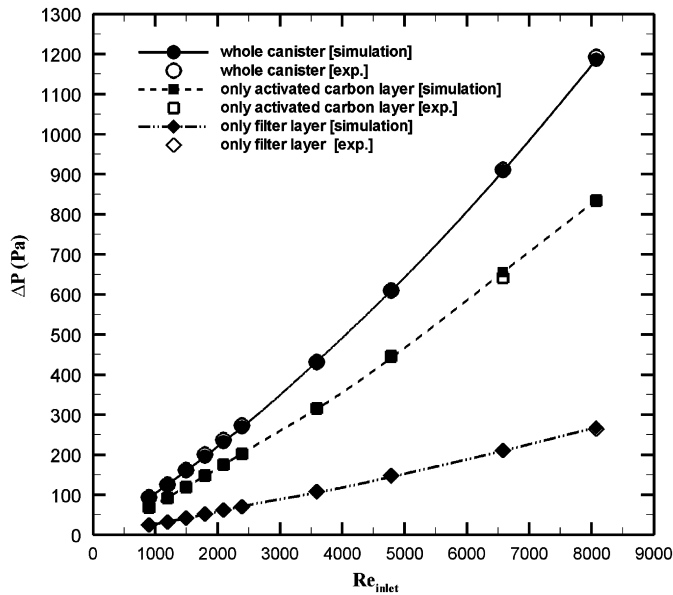**Fig. 6.** Comparison of simulated and experimental results in two porous medium regions and throughout canister for various Re_{inlet} numbers.
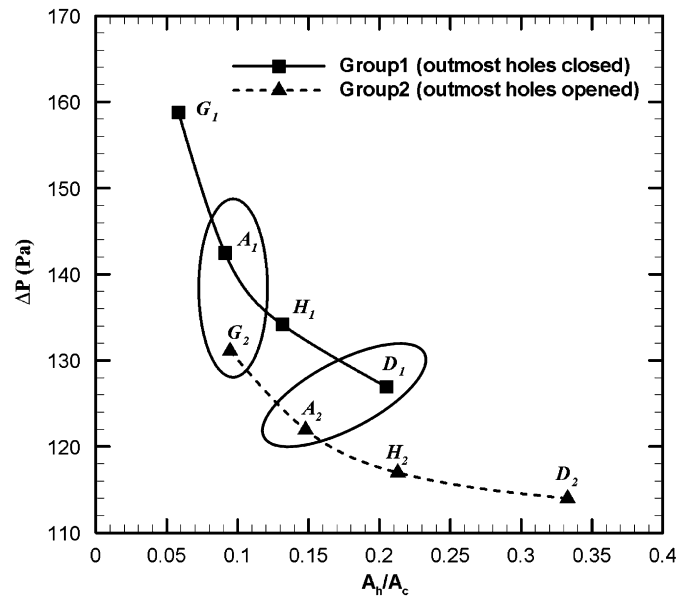

Fig. 8. Relationship between change in hole area and pressure drop in activated carbon layer.
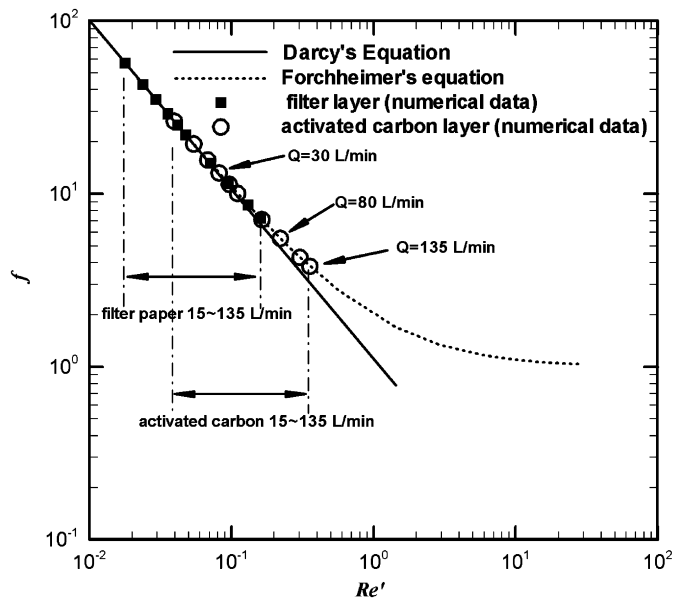

Fig. 7. f–Re' relationships for filter and activated carbon layer.

Similar coefficients for the activated carbon layer can then be obtained:

$$\alpha_2 = 2.39 \times 10^9 \, \text{m}^{-2}, \quad \beta_2 = 3.21 \times 10^4 \, \text{m}^{-1}.$$

The characteristics of the filter layer and the activated carbon layer are assumed to be homogeneous and isotropic in CFD simulations. Fig. 6 shows that the simulated pressure drops are very close to the experimental values.

Fig. 7 shows the f–Re' relationship for the filter and activated carbon layers at inhalation rates of 15–135 L/min (inlet Reynolds numbers approx. 900–8100). The filter layer exhibits quasi-linear (Darcy's equation) porous medium characteristics. Similarly, the activated carbon layer exhibits linear behavior (viscosity effect) at a flow rate of 30 L/min. As the inhalation rate increases, non-linear be-

havior (inertial effect) gradually appears. However, the porous flow in the activated carbon layer still exhibits a slight inertial effect even at a maximum flow rate of 135 L/min.

3.3. Hole distribution and area of main sieve diaphragm

For a given thickness of the activated carbon layer, the test models were divided into two groups (models A_1, D_1, G_1 and H_1 vs. models A_2, D_2, G_2 and H_2, refer to Table 2) to examine the effect of the distribution and area of holes in the main sieve diaphragm on the pressure drop across the activated carbon layer and flow structure. Fig. 8 plots the relationship between the pressure drop and A_h/A_c at a flow rate of 30 L/min (where A_h represents the hole area for the main sieve diaphragm, and A_c represents the cross-section area, equal to the area of the main sieve diaphragm). The A_h/A_c ratio of each model is between 0.06 and 0.33, with a value of about 0.09 for the prototype canister model A_1 and 0.33 for model D_2. The pressure drop for these two groups decreased as the A_h/A_c value increased, revealing that an increase in the hole area can reduce the pressure drop for a given hole distribution. The pressure drop for model D_2 is approximately 113 Pa, which is 30 Pa lower than the 143 Pa value for model A_1. The hole areas in models A_1 and G_2 are approximately equal, but the difference between their pressure drops is 13 Pa. Even though the area in model D_1 with sealed outermost holes exceeds that in model A_2, the pressure drop in model D_1 is approximately 5 Pa higher than model A_2 with open outermost holes. This result reveals that the effect of the hole distribution on the pressure drop of the activated carbon layer exceeds the effect of the hole area.

Fig. 9(a)–(d) plots velocity contours on an azimuthal angle of 22.5° plane for models A_1, D_1, A_2 and D_2 at a flow rate of 30 L/min. Since the outermost holes are sealed and the porous flow causes momentum loss, the gas flowing through the open holes of the main sieve diaphragm does not easily flow past the outer part of the activated carbon layer, as Fig. 9(a) and (b) indicates. Thus, a larger low-velocity zone forms in this region. Since the hole size of model A_1 is smaller than that of model D_1, the local velocity of gas near the open holes in model A_1 is also greater than that in model D_1. The flow structures of these two models are similar except for the locations of the open holes on the main sieve diaphragm. Fig. 9(c)
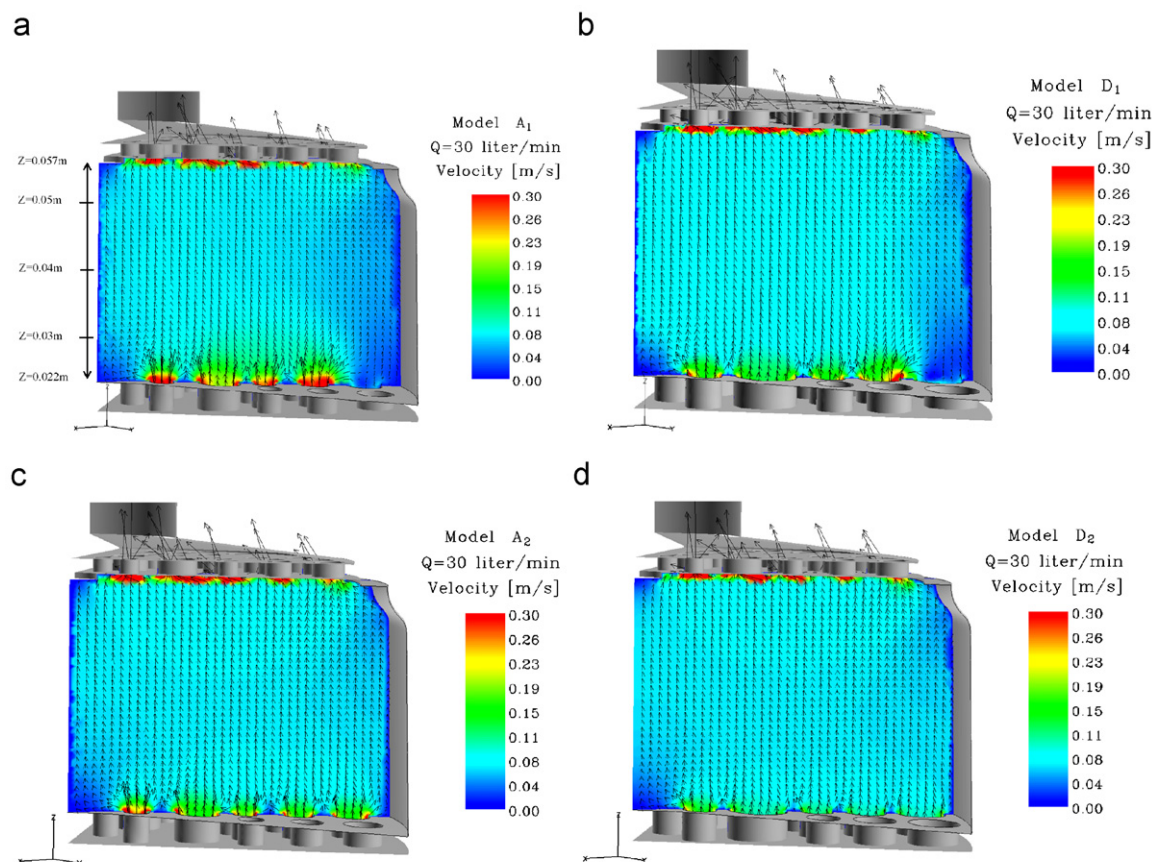
Fig. 9. Velocity contours of activated carbon layer of: (a) model A_1, (b) model D_1, (c) model A_2 and (d) model D_2 at flow rate of 30 L/min.

and (d) shows that once the outermost holes in models A_2 and D_2 are opened, the low-velocity region decreases markedly in size. The flow structures of the two models are also similar. Fig. 10(a)–(c) plots the velocity–position relationship for models A_1, D_1, A_2 and D_2 on a tangential plan view at an azimuthal angle of 22.5°. Fig. 9(a) marks three axial positions of the activated carbon layer ($z = 0.03$, 0.04 and 0.05 m). Fig. 10(a) shows a non-uniform velocity profile for models A_1 and D_2 at $z = 0.03$ m when the outermost holes of main sieve diaphragm are sealed. The hole distributions for models A_1 and D_2 drive the gas passing through the open holes to generate a high-velocity zone where the velocity exceeds the mean velocity V_{ave} ($V_{ave} = Q/A_c$). This forms a low-velocity zone since the gas does not flow smoothly into the region near the wall. The hole area effect leads to a greater local velocity for model A_1 than for model D_1. Models A_2 and D_2 have a more uniform velocity profile than models A_1 and D_1 for open outermost holes and a large hole area. The inertial effect of gas passing through the open holes on the main sieve diaphragm decreases as the flow distance increases. The local high speed flow in models A_1 and D_1 can flow around the outside zone of the activated carbon layer at $z = 0.04$ m (Fig. 10(b)). The velocity profiles of these models at the same hole distribution are quite similar. Fig. 10(c) reveals that the outlet wall around the corner helps form a low-velocity zone near the outlet position ($z = 0.05$ m) on the activated carbon for each test model. All models appear to yield similar velocity profiles at the same hole distribution on the main sieve diaphragm.

This study also compares the velocity–position relationships for models A_1, D_1, A_2 and D_2 at flow rates of 80, 110 and 135 L/min at $z = 0.03$ m. A comparison of Fig. 11(a)–(c) with Fig. 10(a) shows

that the velocity profiles are quite similar in terms of the relative positions of the local high and low velocity zones, and the types of flow. The flow rate barely affects the velocity profile in the activated carbon layer because the porous medium of that layer exhibits quasi-linear behavior in this flow range. The high loss of momentum in activated carbon layer also causes flow changes in the flow in this range that hardly affect the flow behavior, which is dominated by the hole distribution on the main sieve diaphragm.

Figs. 7, 9–11 reveal that the porous flow behavior in the activated carbon layer does not change markedly at inhalation rates from 15 to 135 L/min. The local flow structure changes for the test models clearly occur in the region near the main sieve diaphragm as the gas flows through the holes. The type of passageway on the main sieve diaphragm dominates the flow structure in the activated carbon layer. Moreover, any given hole distribution yields similar flow structures in test models. Forchheimer's equation for a porous medium describes the relationship between the superficial velocity and the pressure drop from a macro perspective. A higher superficial velocity corresponds to a greater pressure drop. According to the continuity equation, the product of the superficial velocity and the flow-through area gives the volumetric flow rate, and the flow-through area does not equal the cross-sectional area of the activated carbon layer. Consider model A_1 as an example: the poor hole positions on the main sieve diaphragm yield a non-uniform velocity profile for the intake gas. Gas does not flow easily into the resulting low-velocity zone, which creates a dead zone and reduces the flow-through area. This increases the superficial velocity in the activated carbon layer, which in turn increases the pressure drop. In contrast, a better hole distribution yields a more uniform velocity profile for
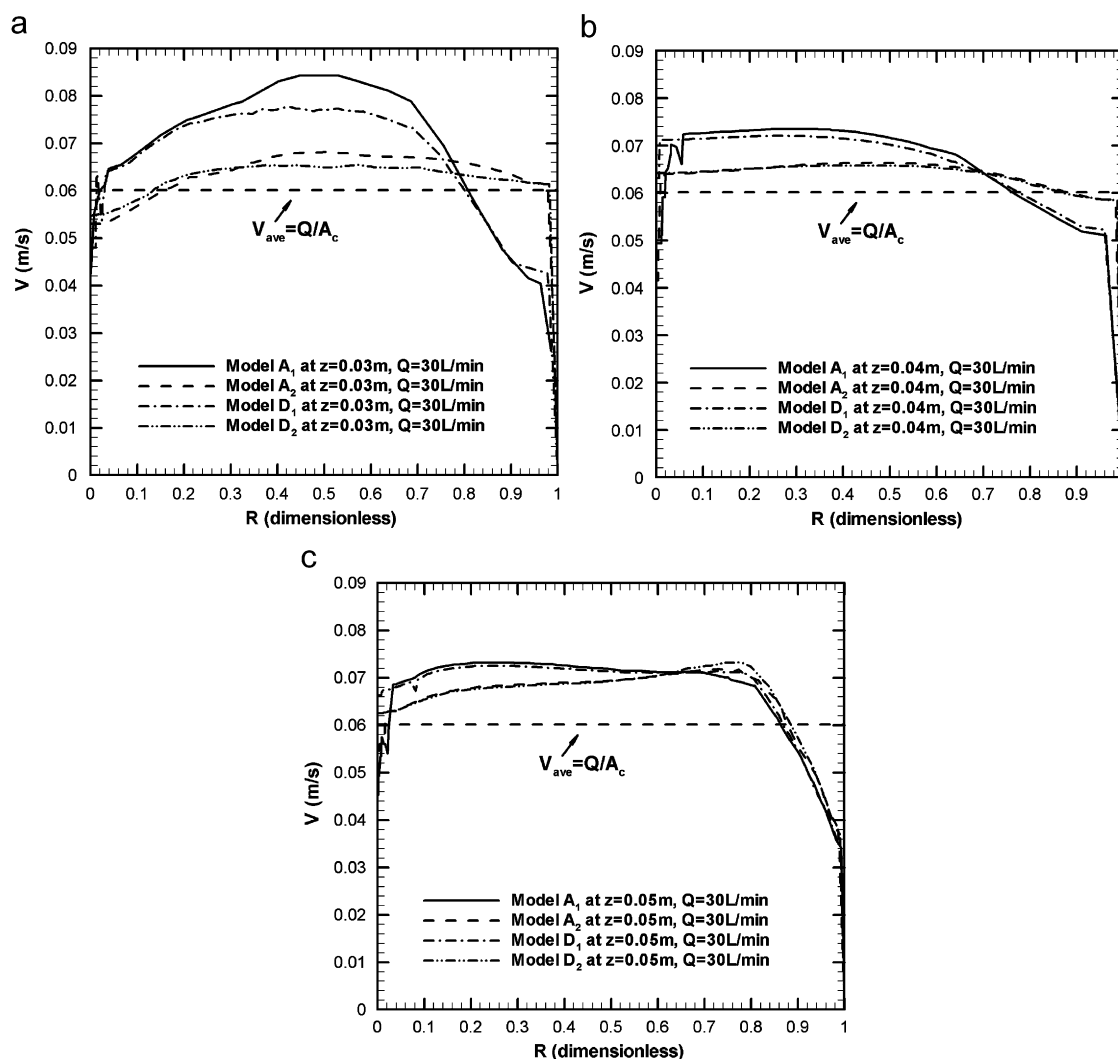
Fig. 10. Velocity profile of models A_1, A_2, D_1 and D_2 at 30 L/min: (a) $z = 0.03$ m, (b) $z = 0.04$ m and (c) $z = 0.05$ m ($\theta = 22.5°$).

the intake gas. In model D_2, for example, increasing the flow-through area reduces the size of the dead zone and the superficial velocity in the activated carbon layer, thereby reducing the pressure drop.

In fact, it is difficult to estimate the area of the actual dead zone of each model in detail. The pressure drop values in Fig. 8 and Eq. (10) can be used to estimate the superficial velocity V_s in the activated carbon layer in each model. The flow-through area in the activated carbon layer at a constant flow rate of 30 L/min can also be calculated. This area is defined as the effective flow-through area A_{eff}. The term A_{eff}/A_c is the ratio of the effective flow-through area to the total area, and $1 - A_{eff}/A_c$ is the proportion of the flow-through area that is ineffective. Moreover, $A_c - A_{eff}$ represents the area of no flow-through, called the dead zone. Fig. 12 shows that model D_2 has an effective flow-through area of about 86% and a dead zone of 14%. The prototype model A_1 has an effective flow-through area of about 70% and a dead zone of 30%. This wastes the activated carbon layer and reveals design flaws. Although the total area of holes in models A_1 and G_2 is quite similar, the difference in hole distributions results in different flow structures. The effective flow-through area of model G_2 (~75%) is 5% greater than that of model A_1. According to the index defined above, the size of the dead zone can be analyzed from a macroscopic viewpoint and compared with the CFD simulation results. Using CFD analysis makes it possible to determine the

effect of the hole distribution and hole area on the flow structure and pressure drop. The positions of the dead zones and the preferential flow can also be identified, which greatly helps improve the design of main sieve diaphragms.

3.4. Activated carbon layer thickness

This section describes how changing the thickness of the activated carbon layer affects the pressure drop. Three non-dimensional thickness values for the activated carbon layer were simulated-full thickness, half thickness, and one-quarter thickness (Table 2). Models were divided into four groups based on the hole distribution and hole area for the main sieve diaphragm. Each group shares the same hole distribution and area, but has a different carbon layer thickness. Group 1 contains models A_1, B_1 and C_1. Group 2 consists of models D_1, E_1 and F_1. Group 3 comprises models A_2, B_2 and C_2. Group 4 consists of models D_2, E_2 and F_2. Fig. 13 plots the relationship between the pressure drop per unit length, the superficial velocity, and the effective flow-through area ratio of the four groups at an inlet flow rate of 30 L/min. Simulation results for all groups show that the superficial velocity and pressure drop per unit length increase and the effective flow-through area ratio decreases as the carbon layer
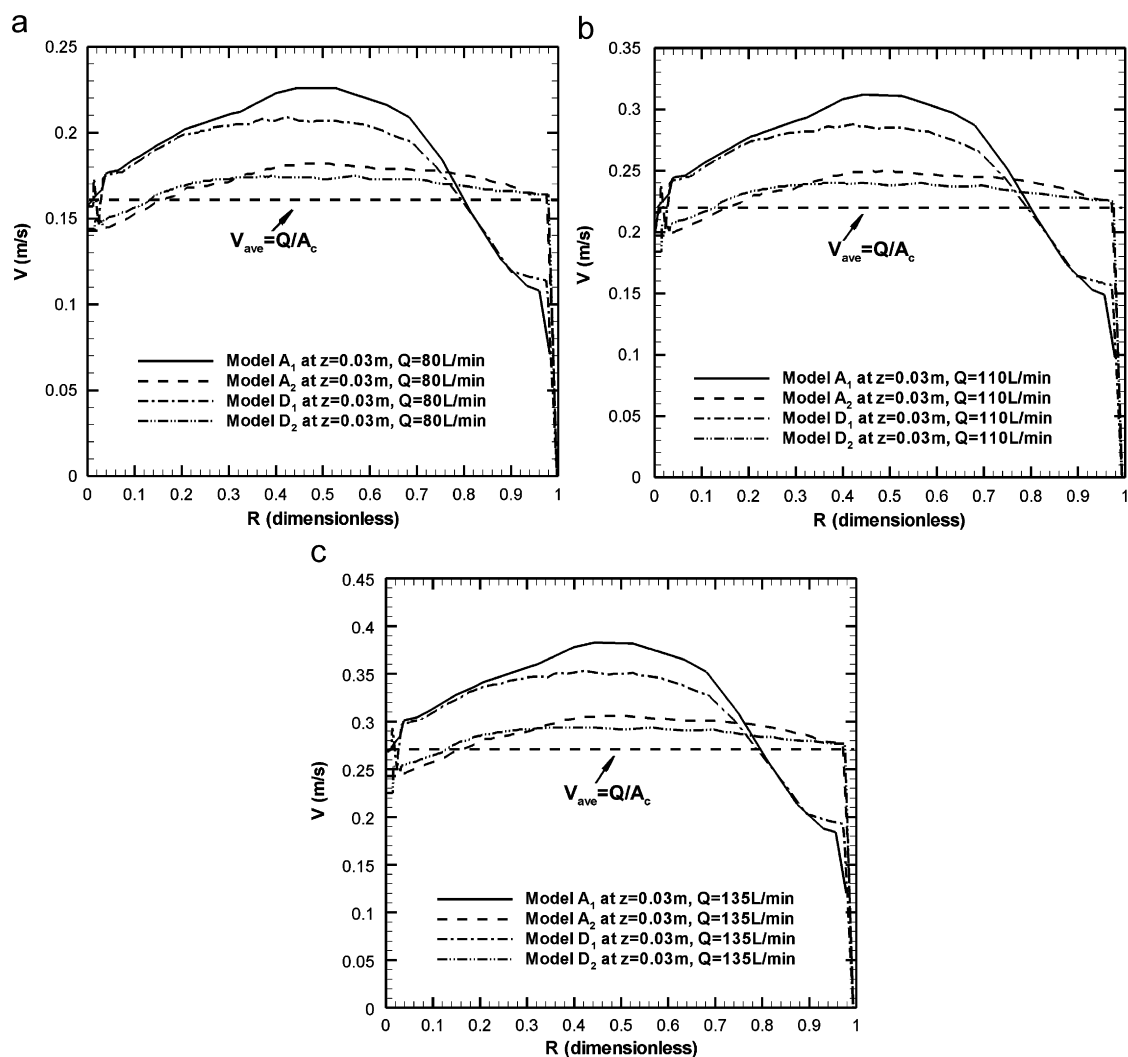
Fig. 11. Velocity profile of models A_1, A_2, D_1 and D_2 at: (a) 80 L/min, (b) 110 L/min and (c) 135 L/min ($z = 0.03$ m, $\theta = 22.5°$).
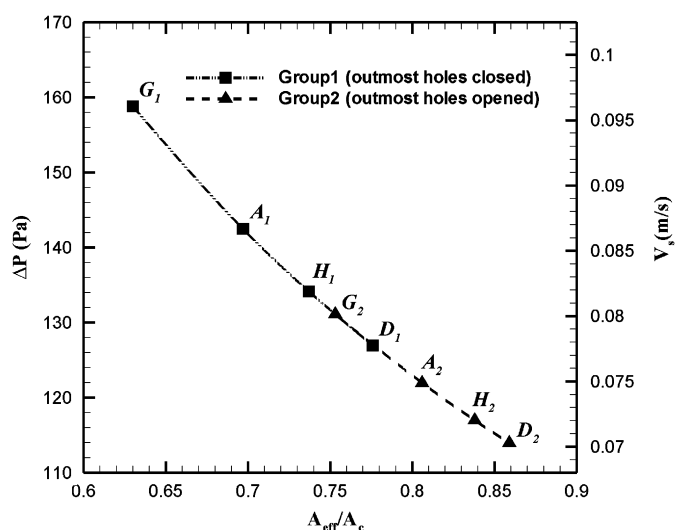

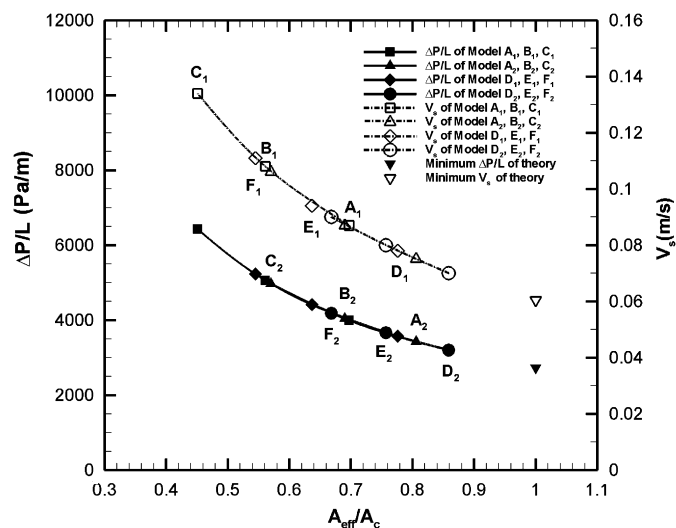**Fig. 12.** Relationship between flow efficiency ratio and pressure drop for the eight models.

Fig. 13. Pressure drop per unit length ($\Delta P/L$) versus superficial velocity (V_s) and effective flow-through ratio at volumetric flow rates of 30 L/min.

thickness decreases. Within Group 1, in which models A_1, B_1 and C_1 share the same sealed outer holes and original hole area, the superficial velocities greatly increases as the thickness decreases. This results from the non-uniform velocity profile generated by the sealed outermost holes. When the thickness of the activated carbon layer decreases, the local high-speed flow will pass quickly through the canister outlet. This result causes the gas not flow around the outside of the activated and to increase the areas of dead zone. The superficial velocity of the Group 4 models, with open outermost holes and a larger hole area, also increases as the thickness decreases. Their

Fig. 14. Pressure drop per unit length ($\Delta P/L$), superficial velocity and effective flow-through ratio at volumetric flow rates of 30, 80, 110 and 135 L/min.

more uniform velocity profiles are associated with a lower change in the pressure drop per unit length. The difference in the pressure drop per unit length, the superficial velocity, and the effective flow-through area for Groups 1, 3 and 2, 4 are attributable to the open hole area. For the original hole positions and the hole areas in Group 1 models A_1, B_1, and C_1 at a flow rate of 30 L/min, the effective flow-through area ratios are approximately 0.7, 0.57, and 0.45, respectively. Group 4 models D_2, E_2, and F_2 have more effective hole distributions and larger holes, with effective flow-through area ratios of approximately 0.86, 0.76, and 0.67, respectively. When the thickness of the activated carbon layer is decreased to one-quarter of its original value, the effective flow-through area and the pressure drop per unit length for model F_2 are approximately equal to those for model A_1. This reveals that the effect of a more uniform hole distribution and a larger hole area on the aerodynamic behavior of the flow can be used to reduce the thickness of the activated carbon layer. As the thickness of the activated carbon layer is attenuated to reduce the distance over which the gas flows, the effect of the hole area becomes more apparent. A more suitable distribution of holes should be used, and the hole area of the main sieve diaphragm should be greatly increased. The effective flow-through areas for test models at flow rates of 80, 110, and 135 L/min are slightly lower than those at 30 L/min, as Fig. 14 shows. Fig. 11(a)–(c) and Fig. 14 reveal that the flow structures of test models, including the velocity profile, the effective flow-through area are barely affected by the flow rate, but are significantly affected by the hole positions and area.
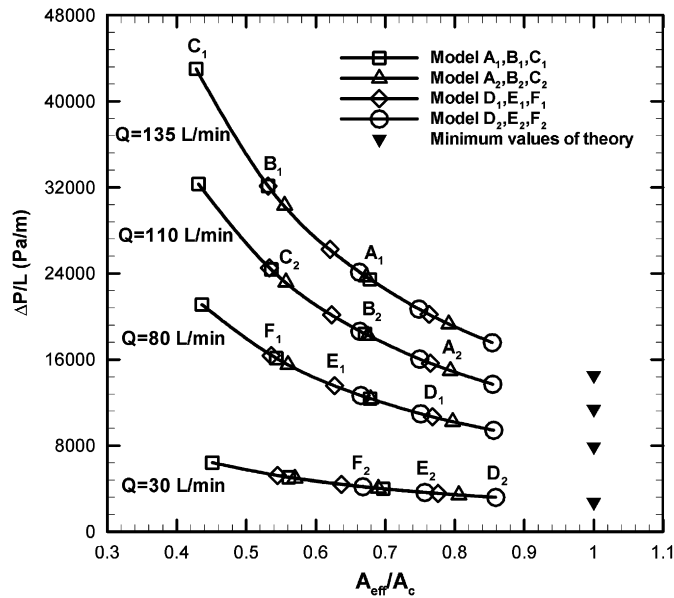
3.5. Air age

To ensure adequate time for filtration and thus improve the canister design, this study considers the residence time of the gas in the activated carbon layer together with the pressure drop. The air age index was used to investigate aerodynamic behavior within the canister. The definition of air age is the local mean age of the fluid, or local mean residence time, which is the average time that a fluid
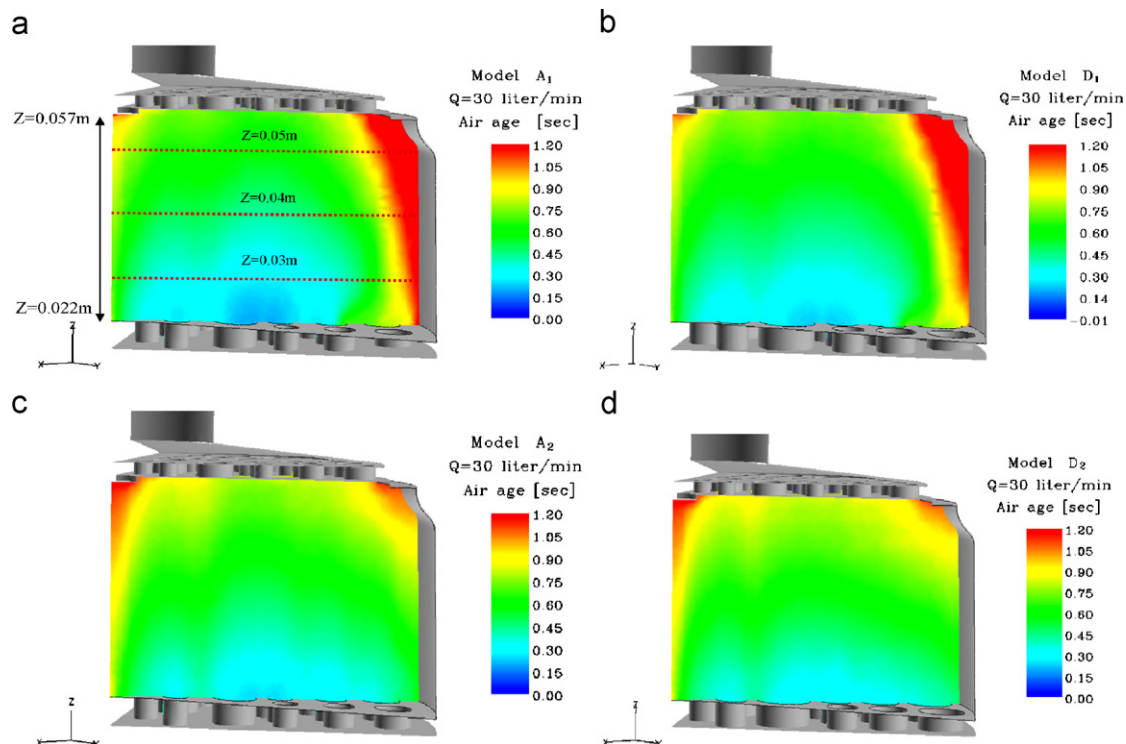

Fig. 15. Air age contours for activated carbon layer in: (a) model A_1, (b) model D_1, (c) model A_2 and model D_2 at $Q = 30$ L/min, $\theta = 22.5°$.
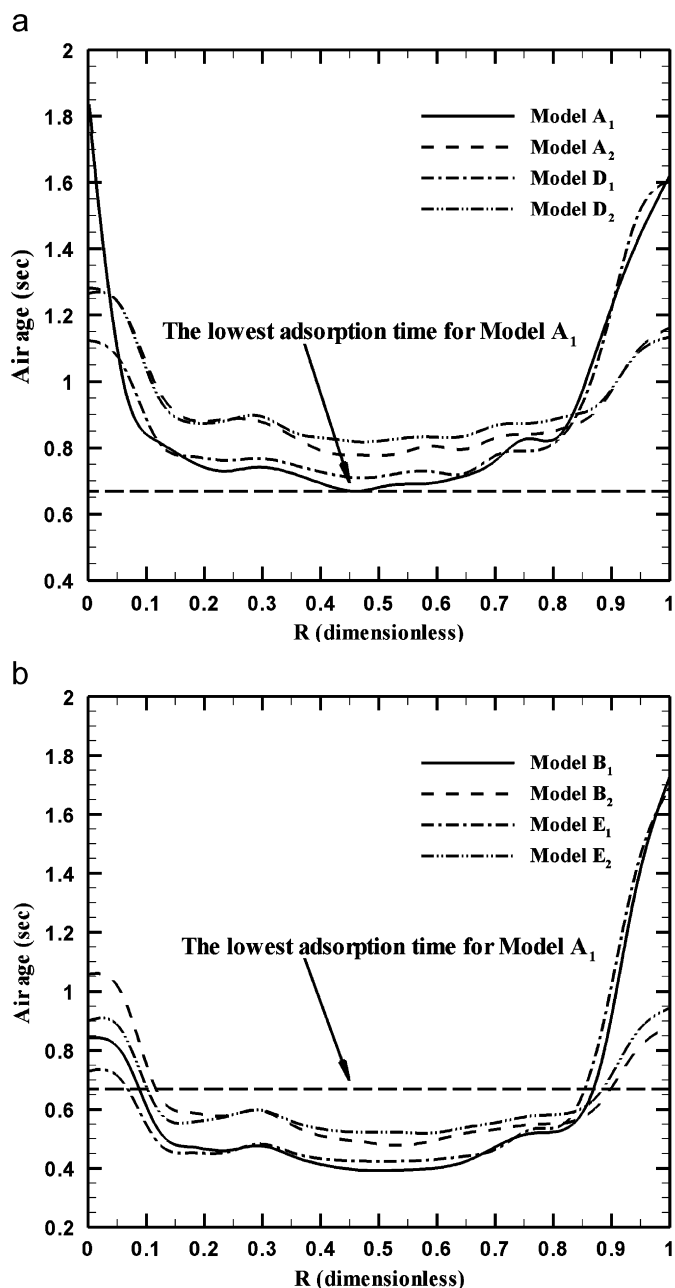
a

b

Fig. 16. Air age distribution for: (a) models A_1, A_2, D_1 and D_2 and (b) models B_1, B_2, E_1 and E_2 (outlet surface of activated carbon layer, $\theta = 22.5°$).

particle takes to reach any point of the domain from the canister inlet. The value of air age index is calculated from Eq. (6). The advantage of displacing adsorption time by the air age index is that complex transient adsorption modes must no longer be solved, greatly reducing computation time.

A greater air age within the activated carbon layer represents a longer residence time and thus a greater chance for adsorption. However, a long air age means that the air has difficulty flowing through the space, and thus forms a dead zone. Using the flow variable distributions described by the air age index makes it much easier to determine the position of dead zones by observing the flow structure within the activated carbon layer. The more difficult alternative to this approach is to use the velocity profile.

Fig. 15(a)–(d) shows the air age contours for models A_1, D_1, A_2, and D_2 at an azimuthal angle of 22.5° and a flow rate of 30 L/min.

Models A_1 and D_1, with sealed outermost holes, clearly have a large zone of higher air age outside the activated carbon layer (Fig. 15(a) and (b)). The gas cannot flow easily through this zone, and a dead zone is formed. The position and size of the dead zones in the two models are almost identical. Other than the difference between air ages near the holes of the main sieve diaphragm, the flow structures in other zones for models A_1 and D_1 exhibit similar air-age distributions since they share the same hole distribution.

Fig. 15(c) and (d) compares models A_2 and D_2 (open outermost holes) to models A_1 and D_1. The original dead zone apparently shrinks after open outermost holes. Models A_2 and D_2 have a larger dead zone at the center of the outlet cross-section surface than models A_1 and D_1 as the fluid flows toward the outer zones. Even if the flow structures of models A_2 and D_2 were the same, the different hole areas would produce differences in the air age near the holes of the main sieve diaphragm. In other zones, the same hole distribution creates similar air age distributions.

Fig. 16(a) plots air age vs. position for models A_1, D_1, A_2 and D_2 at the outlet surface of the activated carbon layer at an azimuthal angle of 22.5°. Model A_1 is a commercial product that passes the filtration test and has the shortest air age of ∼0.67 s. An air age of $\geqslant 0.67$ s corresponds to an adsorption time that meets the filtration standard. The air ages for models A_2, D_1 and D_2 are > 0.67 s and therefore also meet the standard. At the outlet of the activated carbon layer, the air age distributions for models A_2 and D_2 are greater than those for models A_1 and D_1. The air ages in the middle part are slightly larger than ∼0.2 s, representing an increase in adsorption time that corresponds to a more effective filtration of toxic gases.

Fig. 16(b) plots air age vs. position for models B_1, B_2, E_1, and E_2. The air age in most cases is < 0.67 s, indicating that these models would fail the standard adsorption time test. Taken together, the air age data and the previous computational results identify the total dead zone and the positions of local dead zones. These finding provide a useful reference for designing an optimal main sieve diaphragm for gas mask canisters.

4. Conclusions

This paper combines flow visualization techniques, pressure drop measurements, and CFD tools to investigate a gas mask canister with a complex inner configuration of two porous materials. Equations for porous media yield parameters that affect the inner flow aerodynamics in the canister body, including the distribution and area of holes in the main sieve diaphragm and the thickness of the activated carbon layer. These findings help pinpoint areas for improvement in a prototype canister.

The simulation results reveal that the channel design of the main sieve diaphragm dominates the aerodynamic behavior of the fluid within the activated carbon layer. Hole distribution in the main sieve diaphragm determines the flow structures of the activated carbon layer. Changes in the flow rate do not readily affect the flow structure. Better hole distribution and a larger hole area correspond to a lower pressure drop, a smaller dead zone, and a higher adsorption time. However, the structural strength of the main sieve diaphragm must help support the weight of the activated carbon layer in highly dynamic situations. Deformation that results in a loss of activated carbon particles causes the canister to malfunction. Hence, the hole position distribution should be optimized by considering not only how to reduce the pressure drop and the weight of the main sieve diaphragm, but also the structural strength and the limitations of the manufacturing technique used.

The air age can be combined with a defined index, such as the effective flow-through area ratio (A_{eff}/A_c), the ineffective flow-through area ratio ($1-A_{eff}/A_c$), or the area of the dead zone (A_c-A_{eff}), to identify the size of the entire dead zone, the position of local dead zones

and whether or not the adsorption time meets the NIOSH 99.97% standard for filtering toxic gases. The results of this study provide a valuable reference for designing channels in the main sieve diaphragm, and will be helpful in designing gas mask canisters. The parameter analysis herein reveals that the development of a gas mask canister with a low respiratory drop is feasible.

Notation

A_c	cross-section area, m^2
A_{eff}	flow-through area, m^2
A_h	hole area of main sieve diaphragm, m^2
f	friction factor
g_i	gravitational acceleration in the i direction, $m\,s^{-2}$
L	porous medium length, m
p	pressure, Pa
Q	volumetric flow rate, $m^3\,s^{-1}$
R	dimensionless of canister's radius
Re'	modified Reynolds number
Re_{inlet}	inlet Reynolds number
S_i	source term which describes the pressure gradient caused in porous medium, $Pa\,m^{-1}$
u_i	velocity component in the i direction, $m\,s^{-1}$
V_{ave}	average velocity, $m\,s^{-1}$
V_s	superficial velocity, $m\,s^{-1}$

Greek letters

α	viscous parameter of porous material, m^{-2}
β	inertial parameter of porous material, m^{-1}
Δ^P	pressure drop, Pa
Δ^τ	air age increase, s
ε	turbulent dissipation rte, $m^2\,s^{-3}$
κ	permeability of porous material, m^2
μ_{eff}	effective dynamic viscosity, Pa s
μ_l	molecular dynamic viscosity, Pa s
μ_t	turbulent dynamic viscosity, Pa s
ρ	density, $kg\,m^{-3}$
$\overline{\rho u_i' u_j'}$	Reynolds stresses, Pa
σ_τ	turbulent Schmidt number
τ	air age, s
τ_{ij}	viscosity stress tensor, Pa

Appendix A. Supplementary material

Supplementary data associated with this article can be found in the online version at doi:10.1016/j.ces.2009.01.009.

References

Andrada Jr., J.S., Costa, U.M.S., Almeida, M.P., Makse, H.A., Stanley, H.E., 1999. Inertial effects on fluid flow through disordered porous media. Physical Review Letters 82 (26), 5249–5252.

Baléo, J.N., Le Cloirec, P., 2000a. Numerical simulation of the spatial distribution of mean residence time in complex flow through porous media. Progress of Theoretical Physics 138 (Suppl.), 690–695.

Baléo, J.N., Le Cloirec, P., 2000b. Validing a prediction method of mean resident time spatial distributions. A.I.Ch.E. 46 (4), 675–683.

Baléo, J.N., Subrenat, A., Le Cloirec, P., 2000. Numerical simulation of flows in air treatment devices using activated carbon cloths filters. Chemical Engineering Science 55, 1807–1816.

Chen, D.R., Pui, D.Y.H., Liu, B.Y.H., 1995. Optimization of pleated filter designs using a finite-element numerical model. Aerosol Science and Technology 23 (4), 579–590.

Dhaniyala, S., Liu, B.Y.H., 1999. An asymmetrical, three-dimensional model for fibrous filters. Aerosol Science and Technology 30 (4), 333–348.

Dullien, F.A.L., 1979. Porous Media−Fluid Transport and Pore Structure. Academic Press, New York.

Fischetti, M., 2002. Breathing easier? Scientific American 286 (1), 88–89.

Jones, W.P., Launder, B.E., 1973. The calculation of low-Reynolds-number phenomena with a two-equation model of turbulence. International Journal of Heat and Mass Transfer 16, 1119–1130.

Li, X.T., Li, D.N., Yang, X.D., Yang, J.N., 2003. Total air age: an extension of the air age concept. Building and Environment 38, 1263–1269.

Liu, Z.G., Wang, P.K., 1996. Numerical investigation of viscous flow fields around multi-fiber filters. Aerosol Science and Technology 25 (4), 375–391.

Patankar, S.V., 1980. Numerical Heat Transfer and Fluid Flow. Hemisphere Publishing Corporation, Washington.

Subrenat, A., Baléo, J.N., Le Cloirec, P., 2000. Analysis of pressure drops in pleated activated carbon cloth filters. Journal of Environmental Engineering 156 (6), 562–568.

Subrenat, A., Baléo, J.N., Le Cloirec, P., 2001. Electrical behavior of activated carbon cloth heated by the Joule effect. Carbon 39, 707–716.

Subrenat, A., Bellettre, J., Le Cloirec, P., 2003. 3-D numerical simulations of flow in a cylindrical pleated filter packed with activated carbon cloth. Chemical Engineering Science 58, 4965–4973.

Thomas, D., Contal, P., Renaudin, V., Penicot, P., Leclerc, D., Vendel, J., 1999. Modelling pressure drop in HEPA filters during dynamic filtration. Journal of Aerosol Science 30 (2), 235–246.

Wang, F., Wang, X.F., 2003. The effect and adaptation of filtering respirators for physiological function. Journal of PLA Institute of Physical Education 22 (4), 76–78.